Determination of Bubble Size Distributions in Bubble Columns Using LDA

Amol A. Kulkarni and Jyeshtharaj B. Joshi
Institute of Chemical Technology, University of Mumbai, Matunga, Mumbai 400 019, India

Doraiswami Ramkrishna
School of Chemical Engineering, Purdue University, West Lafayette, IN 47907

DOI 10.1002/aic.10274
Published online in Wiley InterScience (www.interscience.wiley.com).

A new method is developed for the determination of bubble size distributions from experimental laser Doppler anemometry (LDA) data through simultaneous measurement of only two orthogonal velocity components and the intermittent time gaps arising out of bubbles passing through the measurement point. An experimentally verifiable assumption of axisymmetry allowed the calculation of the three-dimensional velocity distributions from the two-dimensional measurement through the elegant use of a mathematical transform called Abel's transform. In conjunction with the use of probability theory, it allows calculation of the chord length distribution. The bubble size distribution is obtained by an inversion procedure, which facilitates the transformation of chord lengths to bubble sizes. The inversion procedure is successfully tested with Monte Carlo simulations, in which bubbles of prescribed size distribution were generated for obtaining synthetic data on subtended chord lengths at any given point in the column. It is unambiguously demonstrated that assumptions that do not account for correlation between bubble size and direction of motion can yield highly erroneous size distributions from chord length data. The procedure was then used on experimental chord length distributions obtained using LDA to estimate local bubble size distributions in our bubble column. It is particularly interesting to observe that the mean bubble size estimated from the calculated bubble size distributions were consistent with an estimation based on slip velocity information in accord with the Zuber–Findlay drift flux model. © 2004 American Institute of Chemical Engineers *AIChE J,* 50: 3068–3084, 2004
Keywords: LDA, bubble columns, multi-phase flow, statistical analysis

Introduction

In this article, we are concerned with the measurement of bubble size distributions in bubble columns. The accomplishment of this measurement is envisaged by measuring chord length distributions and transforming them to size distributions. This transformation is profoundly influenced by the direction of bubble motion. Further complexities lie in the bubbles being of nonspherical (anisotropic) shapes, which can rotate (and even oscillate) in nonuniform flow fields, thus further complicating the dependency of chord length on bubble size (radius). The geometrical relationship of chord length to radius requires complete specification of the direction of bubble motion as it moves through the measurement point. Santana and Macias-Machin (2000) present an analysis that uses the availability of the direction of bubble motion to relate chord length to bubble radius. The foregoing work overcomes inaccuracies involved in the inference of bubble sizes from chord lengths in works

Correspondence concerning this article should be addressed to J. B. Joshi at jbj@udct.org or to D. Ramkrishna at ramkrish@ecn.purdue.edu.

that neglect directional variations in bubble motion, as for example in those of Clark and coworkers (1988, 1995, 1998) and Werther (1974). (On the other hand, Santana and Macias-Machin (2000) consider ellipsoidal shaped bubbles that, in rising in different directions, maintain a fixed orientation, an assumption that is at least as unrealistic as allowing bubbles to move only vertically.)

Before discussing our methodology of yielding the bubble size distribution, here we critically review some of the experimental techniques that are used for the measurement of bubble size distribution in a swarm. These techniques are classified as nonintrusive and intrusive measurement techniques. Among the commonly used nonintrusive methods are the photographic/stroboscopic studies (Calderbank, 1958; McLaughlin and Rushton, 1973; Polli et al., 2002), whereby the mean bubble size is obtained from the distribution analysis of the images/photographs. Because the photographic method mainly depends on the refractive index of the liquid and it has bias toward recording bubbles in the wall region, it is not suitable for opaque systems. Second, in the systems with curved surfaces (that is, cylindrical bubble column) the bubble dimensions and the shapes are altered to some extent as a result of curvature refraction yielding a different size and shape, which exert different effects on different sizes. The limitation of bias toward the near-wall bubbles can be overcome through X-ray photography for opaque systems (Rowe and Matsuno, 1971). This method basically gives excellent pictures of complete size distribution in the column, except for the facts that: (1) at high gas throughputs, it becomes difficult to identify and isolate different bubbles from the picture; and (2) the X-rayed width of the bed is limited by the available ray intensities. Stravs and Stockar (1985) used an ultrasound pulse transmission technique for the systems where the optic-based methods fail. The basic principle is that the ultrasound of a particular frequency, when traveling through a multiphase system, becomes attenuated and loses energy upon encountering obstacles and generates a pulse upon reaching the transducer. This sound-pressure pulse is amplified and used as the information tool for the characterization of the obstacle (that is, bubbles).

Another nonintrusive in situ method, based on the analysis of data obtained by laser Doppler anemometry (LDA) (Kulkarni et al., 2001c) or infrared Doppler anemometry, gives the local bubble rise/slip velocities that, with appropriate knowledge about the relationship between bubble size and rise velocity, yields bubble size distribution. The correctness in this kind of analysis depends on the accuracy of the relationship between size and velocity. The second class of measurement technique uses intrusive probes and it has a wide applicability in industries. Under this category, a large number of techniques are used and have distinct advantages over the nonintrusive methods. One of the most important is its ability to obtain the local information. These include capacitance probes, resistance/impedance probes, electroresistivity probe, conductivity probes, optical probes and static pressure probes.

A detailed review of the intrusive and nonintrusive measurement techniques and their applicability in the single-phase and two-phase systems are reported in the work of Cheremisinoff (1986) and Boyer et al. (2002). It should be noted that the information obtained from different intrusive techniques yields the chord length distribution and with increasing number of probe tips, inferring the bubble size/shape becomes more accessible. Much of the analysis uses only a single-tip probe that would yield information about the chord lengths, which are later transformed into bubble size distribution under assumed shapes. However, in reality, both the size distribution and shape distribution must be accounted for, and the situation does not give justice to the analysis based on fixed shapes (Lim and Agarwal, 1990). Further, it even becomes important to address the direction of motion of bubble, which needs further measurement accuracy in terms of either a greater number of probe tips or a combination of double optical probes and imaging (Kiambi et al., 2003), followed by a image reconstruction and shape analysis. However, the limitations of imaging do not allow the use of this method at relatively high gas throughputs. Thus, in such a situation, the analysis can be worked out by using the information about all three components of velocity of bubble and the time it takes to pass through the measurement point, which thus far has not been tried to elucidate the bubble motion in a swarm. Another way for the estimation of bubble size distribution is to formulate an efficient strategy for transformation of the measured chord length distribution to the bubble size distribution (Liu and Clark, 1995; Liu et al., 1998).

The above-mentioned possibility of measuring all three components of bubble velocity can be used to reconstruct the bubble size distribution in an efficient manner. In the present work, however, we were constrained to measure velocity distributions along only two perpendicular directions, which do not permit an exact assessment of even the actual chord length. This constraint was mainly because of the available nonintrusive experimental facility (three-beam LDA). Using a three-beam LDA, we can simultaneously measure only two velocity components, and in a bubbly flow, it appears most difficult for a five-/six-beam LDA system to form a measurement volume by intersection of all the beams without any bubble–beam interaction of at least one of them. Thus, it would make it difficult to measure all three velocity components simultaneously. Thus, with a nonintrusive measurement facility in bubbly flows, it is required to develop an approach that would be capable of overcoming the foregoing instrumental lacunae. Because the passage of bubbles will interrupt the flow of liquid through the measurement point, the actual measurement includes the two-dimensional velocity information as well as the data-interruption times.

In the ensuing discussion, we will loosely refer to the foregoing measurement as the "collected data." The velocity data-interruption time multiplied by the magnitude of bubble velocity will of course afford the actual chord length. However, because the collected data do not include the full three-dimensional velocity of passing bubbles, the real chord length is also unavailable. Consequently, we present a fresh analysis of this problem based on a very different perspective from that of Santana and Macias-Machin (2000). This viewpoint introduces symmetry assumptions about the motion of bubbles along with a proposed procedure for experimental verification of the same. The second assumption of axisymmetry implies that the distribution of radial or tangential component of the bubble velocity at any fixed axial plane is only a function of the radial coordinate ρ. Moreover, from the experimental measurements it turns out that the distributions are the same for both the radial component and the tangential component of the bubble velocity. This symmetry assumption allows one to overcome the deficiency in measurement to convert the collected data to

chord length distributions, which are in turn converted to actual size distributions. We demonstrate the validity of the symmetry assumptions for the data collected from our bubble column. The presence of such symmetry simplifies the task of the experimenter in that two-dimensional (2-D) distributions suffice to obtain the complete 3-D perspective required for converting chord length distributions to bubble size distributions.

In view of the foregoing discussion, we have presented a systematic investigation of this problem in the following sections. In the section on theoretical formulation of inverse problem, we initially discuss the probability distributions for bubble motion as well as the random period of interruption of laser data, denoted T, as bubbles interrupt liquid motion through the measurement point. Two different descriptions of the random velocity vector above are used, the reason for which will soon become apparent. The first, in conjunction with T, uses the velocity components in cylindrical polar coordinates for the bubble column with the vertical axis (ζ) coinciding with the column axis, perpendicular to which lie the radial and tangential coordinates, and is used because it can naturally accommodate certain conditions of axisymmetry. The second transforms T to chord length L, viewing the random velocity vector as made up of the bubble speed (magnitude of its velocity) and direction of motion described by the two azimuthal angles for spherical coordinates mounted on the bubble center, and the actual chord length. The latter coordinate system is more convenient to relate the chord length to the bubble radius. The transformation between the two coordinate descriptions is identified and used for converting the probability distributions from one system to the other. In the next subsection, we introduce important assumptions connected with our development, one of which is concerned with the spatial distribution of spherical bubbles (with center O) around the measurement point (P), and the other is a basic axisymmetric assumption that neglects dependency of all variables with the angle α. (We have been guided by our desire to base our analysis on geometric simplicity associated with spherical bubbles being allowed to move in various directions than to use nonspherical shapes in the presence of restricted directions of motion. In other words, the assumption of freely moving spherical bubbles seemed more appealing than nonspherical bubbles translating without change in orientation!) This is followed by the development of the inversion of chord-length data to bubble size distributions, if the full three-dimensional velocity distribution were available along with the data-interruption times. The subsection after this is concerned with the details of how the deficiency of data implied by the two-dimensional velocity measurement can be overcome. Thus as mentioned earlier, it introduces a second assumption of axisymmetry and elucidates how a mathematical tool called *Abel's transform* (see, for example, Yoshikawa (1998) and Vicharelli and Lapatovich (1987)). can be used to exploit this symmetry of the system to obtain the full three-dimensional velocity distribution and thus the chord length distribution.

The methodology for determination of bubble size distributions is presented in its continuous form as well as in discretized versions, the latter being more convenient for computational procedures in the application of the method. The methodology is tested both on simulated data as well as our own experimental data on bubble size distributions in a bubble column. The use of simulated data was important to test the veracity of the method to facilitate comparison of the extracted size distribution with known size distributions used to generate the data by Monte Carlo simulations. This is accomplished in the section on application of methodology. The use of actual experimental data from our bubble column is discussed in the results and discussion section, which takes due precaution to verify that the assumption of axisymmetry is in fact a reasonable approximation.

Theoretical Development: Formulation of Inverse Problem

Probability density functions: definitions

Let $p_R(r)$ be the distribution of bubble radii. We let the probability distribution for the measured chord length[4] be denoted $p_L(l)$ and the probability distribution for the chord length, conditional on the bubble radius, be denoted by $p_{L\,|\,R}(l\,|\,r)$, which, on application of the total probability theorem, gives the following integral equation

$$p_L(l) = \int_0^\infty p_{L|R}(l|r)\, p_R(r) dr \tag{1}$$

(We make a distinction between the actual chord length and the measured chord length because the latter is actually a projection of the former for the case of bidirectional measurements with three intersecting laser beams.) The conditional probability function $p_{L\,|\,R}(l\,|\,r)$ is governed by considerations of the direction of bubble motion and elementary geometry. Bubbles are viewed to move in random directions through the measurement point, registering chords similar to LDA data (Kulkarni et al., 2001b). It is of interest to first consider how such data can be used to calculate the function $p_{L\,|\,R}(l\,|\,r)$. Note that this function must vanish for $l > 2r$ because the maximum chord length can only be the diameter of the bubble. The relationship between bubble radius and the recorded chord length is addressed here in detail.

We denote by $p_{\Theta\Phi\,|\,R}(\theta, \varphi\,|\,r)$, the conditional probability distribution function for the direction of a bubble's motion, given that it has radius $R = r$. Note that the chord length does not appear among the arguments in this distribution because specification of the direction of bubble motion and bubble radius will uniquely specify the chord length. The conditional distribution $p_{L\,|\,R}(l\,|\,r)$ can be calculated through the total probability theorem, using probability distributions for the relative position of the bubble and the direction of bubble motion. Thus, we may write

$$p_{L|R}(l|r) = \int_0^{2\pi} d\varphi \int_0^{\pi} \sin\theta d\theta \int_0^{2\pi} d\varphi' \int_0^{\pi} \sin\theta' d\theta' \times p_{L|\Theta\Phi R\Theta'\Phi'}(l|\theta, \varphi, r; \theta', \varphi') p_{\Theta\Phi\Theta'\Phi'|R}(\theta, \varphi; \theta', \varphi'|r) \tag{2}$$

where we have used primed coordinates on the azimuthal angles to denote the orientation of the bubble location relative to the point P (Figure 1). The function $p_{L\,|\,\Theta\Phi R\Theta'\Phi'}(l\,|\,\theta, \varphi, r, \theta', \varphi')$ can be identified analytically from geometry. We make two noteworthy assumptions associated with the function

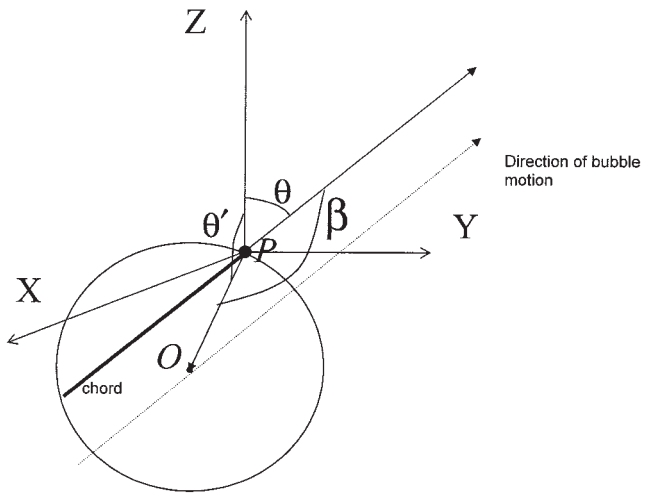

Figure 1. Geometry of reference used in this analysis.

$p_{\Theta\Phi\Theta'\Phi' \mid R}(\theta, \varphi; \theta', \varphi' \mid r)$. One is that the direction of motion is independent of the relative orientation, and the other is that the bubbles are located *uniformly* with respect to point P, which liberates the function $p_{\Theta\Phi\Theta'\Phi' \mid R}(\theta, \varphi; \theta', \varphi' \mid r)$ from explicit dependency on θ' and φ'. The details of the geometric arguments concerning the relationship between bubble size and the length of the chord subtended by a bubble moving in a specific direction are discussed in the next section.

Distributions for bubble location and motion

Geometrical Arguments. The system under investigation is composed of a cylindrical bubble column, where gas dispersed in the liquid is considered to take the form of spherical bubbles moving in various directions, which, understandably, must be correlated to their sizes. We use cylindrical coordinates for specifying bubble location in the column with the coordinate axes represented by (ζ, ρ, α), where ζ represents the axial position of the radial plane constituting point P, ρ denotes the radial distance of P from the column axis, and α is the angle made by the perpendicular from P to the column axis (Figure 1) with a reference line (x-axis) on the horizontal plane. We are concerned with bubbles passing in different directions through a fixed point P in a multiphase flow field, which is analogous to the situation in a bubble column. LDA measurements are made in the bubble column and the data can be processed properly for extracting the velocities of each bubble passing through the measurement point (details are provided in Kulkarni et al., 2001a). As the bubble surface first touches the measurement point P, its orientation as determined by the location of its center relative to P is a random quantity and it is assumed that, during the complete passage of a bubble through the measurement point, its orientation does not change. Let the direction vector of this orientation be given by the azimuthal pair (θ', φ'), whereas the direction of bubble motion may be denoted by (θ, φ), so on a geometrical basis, the angle between the bubble orientation and bubble motion (β), is

$$\cos\beta = \cos\theta\cos\theta' + \sin\theta\sin\theta'\cos(\varphi - \varphi') \qquad (3)$$

A simple geometrical argument now leads to the calculation of the chord length actually subtended (L) by the bubble as $L = 2R\cos\beta$, where R is the bubble radius. From the foregoing geometrical result, the probability distribution $p_{L \mid \Theta\Phi R\Theta'\Phi'}(l \mid \theta, \varphi, r, \theta')$ is obtained as

$$p_{L|\Theta\Phi R\Theta'\Phi'}(l|\theta, \varphi, r; \theta', \varphi') = \delta(l - 2r\cos\beta) \qquad (4)$$

where δ represents the Dirac delta function.

Distribution of Bubble Motion and Its Location. Because the true chord length subtended by a bubble is a function of the actual velocity vector of the bubble motion and the time required for passing through the point P, we associate a probability distribution function $p_{V_\zeta V_\rho V_\alpha T}(v_\zeta, v_\rho, v_\alpha, t)$ for the joint distribution of the axial, tangential, and radial bubble velocities, and the time that is related to the size of the bubble. We have merely suppressed position coordinates in the foregoing distribution rather than to suggest independence from them. However, it is reasonable to expect axial symmetry in the column by which we can eliminate any net dependency of the above probability distribution on the azimuthal angle α, and so we write

$$\left(\frac{\partial p_{V_\zeta V_\rho V_\alpha T}}{\partial\alpha}\right)_{\mathbf{v},t,\zeta,\rho} = 0 \qquad (5)$$

In Eq. 5, which eliminates all *explicit* dependency of the distribution on the angle α, constant **v** implies the constancy of V_ζ, V_ρ, and V_α. Although the cylindrical coordinate frame of reference is natural to refer to different points in the column, it is more convenient to analyze the passage of the bubble through the measurement point using spherical coordinates. Thus the probability distribution $p_{V\Theta\Phi L}(v, \theta, \varphi, l)$ can be defined in spherical coordinates (using spherical coordinates with P as center). (Note that for a *fixed* velocity vector **v** the relationship between its description with respect to ζ, ρ, α coordinates and that with respect to v, θ, φ coordinates depends on the angle α.) Here we are using subtended chord length for the present, although the bubble size is our primary interest. The transformation of coordinates is easily determined to be the following

$$v_\zeta = v\cos\theta \qquad v_\rho = v\sin\theta\cos(\varphi - \alpha),$$
$$v_\alpha = v\sin\theta\sin(\varphi - \alpha), \qquad t = l/v$$

where l is the length of the subtended chord, which can also be readily inverted. The inverse relations are as follows:

$$v = \sqrt{v_\zeta^2 + v_\rho^2 + v_\alpha^2}, \qquad \theta = \tan^{-1}\left(\frac{\sqrt{v_\rho^2 + v_\alpha^2}}{v_\zeta}\right),$$
$$\varphi = \alpha + \tan^{-1}\left[\frac{v_\alpha}{v_\rho}\right], \qquad l = vt \qquad (6)$$

where α is to be regarded as fixed.

To relate the probability distribution $p_{V\Theta\Phi L}(v, \theta, \varphi, l)$ to the distribution $p_{V_\zeta V_\rho V_\alpha T}(v_\zeta, v_\rho, v_\alpha, t)$, we may write

$$p_{V\Theta\Phi L}(v,\ \theta,\ \varphi,\ l) = p_{V_\xi V_\rho V_\alpha T}(v_\xi,\ v_\rho,\ v_\alpha,\ t)\left[\frac{\partial(v,\ \theta,\ \varphi,\ l)}{\partial(v_\xi,\ v_\rho,\ v_\alpha,\ t)}\right]^{-1} \tag{7}$$

where the Jacobean on the right-hand side is readily obtained by calculating its inverse as

$$\begin{bmatrix} \frac{\partial v_\xi}{\partial v} & \frac{\partial v_\rho}{\partial v} & \frac{\partial v_\alpha}{\partial v} & \frac{\partial t}{\partial v} \\ \frac{\partial v_\xi}{\partial \theta} & \frac{\partial v_\rho}{\partial \theta} & \frac{\partial v_\alpha}{\partial \theta} & \frac{\partial t}{\partial \theta} \\ \frac{\partial v_\xi}{\partial \varphi} & \frac{\partial v_\rho}{\partial \varphi} & \frac{\partial v_\alpha}{\partial \varphi} & \frac{\partial t}{\partial \varphi} \\ \frac{\partial v_\xi}{\partial l} & \frac{\partial v_\rho}{\partial l} & \frac{\partial v_\alpha}{\partial l} & \frac{\partial t}{\partial l} \end{bmatrix} = \begin{bmatrix} \cos\theta & \sin\theta\cos(\varphi-\alpha) & \sin\theta\sin(\varphi-\alpha) & -l/v^2 \\ -v\sin\theta & v\cos\theta\cos(\varphi-\alpha) & v\cos\theta\sin(\varphi-\alpha) & 0 \\ 0 & -v\sin\theta\sin(\varphi-\alpha) & v\sin\theta\cos(\varphi-\alpha) & 0 \\ 0 & 0 & 0 & 1/v \end{bmatrix} = v\sin\theta[\cos^2\theta + \sin^2\theta\cos 2(\varphi-\alpha)]$$

which on substitution in Eq. 7 gives

$$p_{v\Theta\Phi L}(v,\ \theta,\ \varphi,\ l) = p_{V_\xi V_\rho V_\alpha T}(v_\xi,\ v_\rho,\ v_\alpha,\ t) \times \{v\sin\theta[\cos^2\theta + \sin^2\theta\cos 2(\varphi-\alpha)]\} \tag{8}$$

Formulation of inverse problem for bubble size distribution

In continuation with the development of defining the *probability density functions*, we use the total probability theorem to express $p_{V\Theta\Phi L}(v,\ \theta,\ \varphi,\ l)$ as

$$p_{V\Theta\Phi L}(v,\ \theta,\ \varphi,\ l) = \int_0^\infty P_R(r)dr \int_0^\pi d\theta' \sin\theta' \int_0^{2\pi} d\varphi' \times p_{V\Theta\Phi L|\Theta'\Phi' R}(v,\ \theta,\ \varphi,\ l|\theta',\ \varphi',\ r)p_{\Theta'\Phi'|R}(\theta',\ \varphi',\ r) \tag{9}$$

The rules of probability allow the density function $p_{V\Theta\Phi L\,|\,\Theta'\Phi' R}(v,\ \theta,\ \varphi,\ l\,|\,\theta',\ \varphi',\ r)$ to be rewritten as

$$p_{V\Theta\Phi L|\Theta'\Phi' R}(v,\ \theta,\ \varphi,\ l|\theta',\ \varphi',\ r) = p_{V\Theta\Phi|\Theta'\Phi' R}(v,\ \theta,\ \varphi|\theta',\ \varphi',\ r) \times p_{L|V\Theta\Phi\Theta'\Phi' R}(l|v,\ \theta,\ \varphi,\ \theta',\ \varphi',\ r) \tag{10}$$

and the term on the right-hand side of Eq. 10 can be simplified under the assumption of the bubble velocity being independent of the relative orientation of the bubble, to obtain

$$p_{V\Theta\Phi|\Theta'\Phi' R}(v,\ \theta,\ \varphi|\theta',\ \varphi',\ r) = p_{V\Theta\Phi|R}(v,\ \theta,\ \varphi|r)$$

Further, from the geometric considerations earlier we obtain

$$p_{L|V\Theta\Phi\Theta'\Phi' R}(l|v,\ \theta,\ \varphi,\ \theta',\ \varphi',\ r) = \delta(l - 2r\cos\beta) \tag{11}$$

The velocity information on the bubble is irrelevant to the prediction of the exact chord length appearing on the right-hand side. Thus, on simplification of Eq. 9 we obtain

$$p_{V\Theta\Phi L}(v,\ \theta,\ \varphi,\ l) = \frac{1}{4\pi}\int_0^\infty P_R(r)drK(\theta,\ \varphi,\ r,\ l)\,p_{V\Theta\Phi|R}(v,\ \theta,\ \varphi|r) \tag{12}$$

where $K(\theta, \varphi, r, l)$ is given by the following expression

$$K(\theta,\ \varphi,\ r,\ l) = \int_0^{2\pi} d\varphi' \frac{1}{2r}\left\{ \chi\left[0 \le \theta < \frac{\pi}{2}\right] H(2r\cos\theta - 1)\left[\cos\theta - \frac{y_-\sin^2\theta\cos^2(\varphi-\varphi')}{\left(\frac{1}{2r} - y_-\cos\theta\right)}\right]^{-1} + \chi\left[\frac{\pi}{2} \le \theta < \pi\right] H(2r\cos\theta + 1)\left[\cos\theta - \frac{y_+\sin^2\theta\cos^2(\varphi-\varphi')}{\left(\frac{1}{2r} - y_+\cos\theta\right)}\right]^{-1} \right\}$$

in which we have set

$$H(x) = \begin{cases} 1, & x \geq 0 \\ 0, & x < 0 \end{cases} \qquad \chi[\theta \in I] = \begin{cases} 1, & \theta \in I \\ 0, & \theta \notin I \end{cases}$$

and

$$y_{\pm} = \frac{1}{2r}\left\{\frac{\cos\theta \pm \sin\theta\cos(\varphi - \varphi') \times \sqrt{\frac{4r^2}{l^2}[1 - \sin^2\theta\sin^2(\varphi - \varphi')] - 1}}{1 - \sin^2\theta\sin^2(\varphi - \varphi')}\right\}$$

The expression for $K(\theta, \varphi, r, l)$ can be achieved with the help of coordinate transformation through Jacobian substituting the expression for $p_{v\Theta\Phi L}(v, \theta, \varphi, l)$. The estimation of bubble size distribution must be accomplished through a solution of Eq. 12.

Overcoming the constraint of two-dimensional velocity measurements

Because we have only two-dimensional velocity measurements from our experiments, it is not possible to use Eq. 12 in estimating the bubble size distributions. Thus, instead of having the 3-D distribution $p_{V_\zeta V_\rho V_\alpha T}(v_\zeta, v_\rho, v_\alpha, t)$, we only have the 2-D distribution $p_{V_\zeta V_\rho T}(v_\zeta, v_\rho, t)$ given by

$$p_{V_\zeta V_\rho T}(v_\zeta, v_\rho, t) = \int_{-\infty}^{\infty} p_{V_\zeta V_\rho V_\alpha T}(v_\zeta, v_\rho, v_\alpha, t)dv_\alpha \qquad (13)$$

To overcome this deficiency, we now introduce another axisymmetric assumption, which implies the following. The probability that the bubble velocity has a given vector **v**, at any fixed radial position from the column axis, cannot depend (explicitly or implicitly) on α along the tangential direction. Using the foregoing transformation, the mathematical representation of the above assumption of axisymmetry is given by

$$\left(\frac{\partial p_{V_\zeta V_\rho V_\alpha T}}{\partial v_\rho}\right)_{v_\zeta, v_\alpha, t}\left(\frac{\partial v_\rho}{\partial \alpha}\right)_{\zeta,\rho} + \left(\frac{\partial p_{V_\zeta V_\rho V_\alpha T}}{\partial v_\alpha}\right)_{v_\zeta, v_\rho, t}\left(\frac{\partial v_\alpha}{\partial \alpha}\right)_{\zeta,\rho} = 0 \qquad (14)$$

Computing the partial derivatives from the transformation, Eq. 6, we obtain

$$v_\alpha\left(\frac{\partial p_{V_\zeta V_\rho V_\alpha T}}{\partial v_\rho}\right)_{v_\zeta, v_\alpha, t} = v_\rho\left(\frac{\partial p_{V_\zeta V_\rho V_\alpha T}}{\partial v_\alpha}\right)_{v_\zeta, v_\rho, t} \qquad (15)$$

Equation 15 may be viewed as a partial differential equation with respect to the dependency on v_ρ and v_α whose solution can be elegantly expressed as

$$p_{V_\zeta V_\rho V_\alpha T}(v_\zeta, v_\rho, v_\alpha, t) \equiv F(v_\zeta, \sqrt{v_\rho^2 + v_\alpha^2}, t) \qquad (16)$$

Equation 16 implies symmetry with respect to the radial and tangential velocities. The measured distribution, from Eq. 13, may therefore be written as

$$p_{V_\zeta V_\rho T}(v_\zeta, v_\rho, t) = \int_{-\infty}^{\infty} F(v_\zeta, \sqrt{v_\rho^2 + v_\alpha^2}, t)dv_\alpha = 2\int_0^{\infty} F(v_\zeta, \sqrt{v_\rho^2 + v_\alpha^2}, t)dv_\alpha \qquad (17)$$

In what follows, we shall show that the measurement of the lefthand side of Eq. 17 can in fact be used to obtain the full distribution in Eq. 16! Toward this end, we convert the integral on the extreme righthand side of Eq. 16 using the transformation $\sqrt{v_\rho^2 + v_\alpha^2} = u$ to

$$p_{V_\zeta V_\rho T}(v_\zeta, v_\rho, t) = \int_{v_\rho}^{\infty} F(v_\zeta, u, t)\frac{2udu}{\sqrt{u^2 - v_\rho^2}} \qquad (18)$$

The left-hand side of Eq. 18 is exactly what has been defined in the mathematical literature as Abel's transform (Abel, 1988) of the unknown function $F(v_\zeta, u, t)$, which can be recovered by the inversion formula

$$F(v_\zeta, u, t) = \frac{1}{\pi}\int_u^{\infty}\left(-\frac{\partial}{\partial v_\rho}p_{V_\zeta V_\rho T}(v_\zeta, v_\rho, t)\right)\frac{dv_\rho}{\sqrt{v_\rho^2 - u^2}} \qquad (19)$$

Interestingly, the assumption of axisymmetry implied by Eq. 14 allows the determination of the complete distribution function $F(v_\zeta, u, t)$ by substituting for u the expression $\sqrt{v_\rho^2 + v_\alpha^2}$ and using Eq. 16. From Eq. 19, however, it is evident that one must get a differentiable fit of the data on the function $p_{V_\zeta V_\rho T}(v_\zeta, v_\rho, t)$, and this part is discussed in the section on application of methodology. To verify whether the experimental data conform to the assumption (Eq. 14) of axisymmetry, we note from Eq. 18 that the 2-D distributions $p_{V_\zeta V_\rho}(v_\zeta, v_\rho)$ and $p_{V_\zeta V_\alpha}(v_\zeta, v_\alpha)$ are the same. Thus by collecting and comparing data for the joint distribution of axial and radial velocities, with that of axial and tangential velocities, the proposed assumption of axisymmetry can be assessed experimentally.

The Solution of Eq. 12

The solution of Eq. 12 may now be considered by using some form of discretization for both the solid angles as well as the bubble sizes. The data are available in the discrete form, which may not be convenient for computation so that one must use a representation in terms of suitably smooth basis functions. Once this representation is available, it can be discretized more conveniently for computational purposes.

Because the subtended chord depends only on the direction of the velocity and not on its magnitude, we may integrate the distribution $p_{V\Theta\Phi L}(v, \theta, \varphi, l)$ over all v in further considerations of Eq. 12. Further, using Eqs. 9 and 16 we obtain

$$p_{\Theta\Phi L}(\theta, \varphi, l) = \int_0^{\infty} p_{V\Theta\Phi L}(v, \theta, \varphi, l)dv$$

$$= \int_0^\infty F(v\cos\theta,\, v\sin\theta,\, v/l) \times \{v\sin\theta[\cos^2\theta + \sin^2\theta\cos 2(\varphi-\alpha)]\}dv$$

where the distribution on the extreme left pertains only to the directional distribution and subtended chord length. Now Eq. 12 can be integrated over all v to obtain

$$p_{\Theta\Phi L}(\theta,\, \varphi,\, l) = \frac{1}{4\pi}\int_0^\infty P_R(r)drK(\theta,\, \varphi,\, r,\, l)\, p_{\Theta\Phi|R}(\theta,\, \varphi|r) \tag{21}$$

To determine the bubble size distribution, it is necessary to appropriately discretize Eq. 21. The unknowns are the discretized versions of the distributions and can be given as

$$p'_{i,k} = \sum_{j=1}^{N_r} a_{i,j,k}p_{i,j} \qquad i = 1,\, 2,\, \ldots,\, N_\omega,\, k = 1,\, 2,\, \ldots,\, N_l \tag{22}$$

where

$$a_{i,j,k} \equiv K(\tilde{\theta}_i,\, \tilde{\varphi}_i,\, \tilde{r}_j,\, \tilde{l}_k) \qquad p'_{i,k} \equiv p_{\Theta\Phi L}(\tilde{\theta}_i,\, \tilde{\varphi}_i,\, \tilde{l}_k)$$

$$p_{i,j} \equiv p_{\Theta\Phi|R}(\tilde{\theta}_i,\, \tilde{\varphi}_i|\tilde{r}_j)\, p_R(\tilde{r}_j)$$

To have closure, we had $N_r = N_l$. Once the unknowns $\{p_{i,j}\}$ are determined we can obtain the bubble size distribution by integration over all the directions of bubble motion

$$p_j = \sum_{i=1}^{N_\omega} p_{i,j} \qquad p_j \equiv p_R(\tilde{r}_j) \tag{23}$$

The discretization of the bubble motion and their sizes can be explained on the basis of certain geometrical arguments. The details are given in Appendix A.

Application of Methodology

The methodology reported in this article was first put to test by using simulated data before they were applied to the measurement of bubble size distributions in the bubble column in our laboratory. Bubbles of a prescribed size distribution were generated by Monte Carlo simulation, whereas the generation of bubble motion was based on two different cases. The first assumed a strong statistical correlation between bubble size and the direction of bubble motion. In the second case, no correlation was assumed between bubble size and direction of motion, which provides an extreme case for verification of our strategy.

In the first case, larger bubbles tended to move vertically, whereas the smaller bubbles were free to move in directions dictated by the local liquid velocity. This correlation between size and direction of motion was derived in a somewhat convoluted way from the data of Nguyen (1998) and our own measurements of bubble motion presented in Appendix B as follows. For any specific bubble size, its vertical rise velocity was obtained from Nguyen's data and the radial and tangential components from the statistics of our data to provide for the directional distribution of bubble motion. The procedure, in more detail, is described below: Because only two velocity components could be measured simultaneously at one location statistical data on the two orthogonal components (v_ρ, v_θ) conditional on v_ζ (for calculation of the direction of bubble motion) will not be available. However, the axisymmety assumption (Eq. 14) can be exploited to generate the required statistics of the direction of motion of bubbles of specified sizes. (To measure the axial–radial and axial–tangential velocity components using a three-beam LDA system, at an equal distance from the axis, it is required to change the location of intersection for the radial and tangential components (although they are in the same plane.) The sensitivity analysis showed that the estimated bubble size distribution remains sufficiently smooth with more than 1500 generated bubbles. Thus for this analysis more than 5000 bubbles were generated (with known distribution), and for every v_ζ the values of v_ρ and v_θ were assigned discretely from the measured range. The bubbles were positioned uniformly in the space surrounding point P and were allowed to travel along the resultant direction. Among all the bubbles, only those passing through point P yielded the chords. Thus, the chord length distribution produced as data was associated with only those bubbles that moved in directions appropriate for subtending chords.

For the second case, bubbles are assumed to move randomly, no specific values of velocity components were assigned to the bubbles conditional on their sizes, and the chord lengths corresponding to the bubble sizes were measured. Now, for the known size and directional distributions, bubbles were allowed to pass through point P and chords were estimated using bubble velocity and passage time as the source information, which is similar to the method adopted while processing the actual data (Kulkarni et al., 2001b). Further, for validation of the model, the resulting chord length distribution was subjected to a series of computational steps:

(1) The statistical data on axial velocity, radial velocity, and interval of data interruption were used to obtain a smooth function to fit them and the function $p_{V_\zeta V_\rho T}(v_\zeta,\, v_\rho,\, t)$. To smooth the data obtained by expanding in terms of basis functions, we set

$$p_{V_\zeta V_\rho T}(v_\zeta,\, v_\rho,\, t) = \sum_{i=1}^{N_\zeta}\sum_{j=1}^{N_\rho}\sum_{k=1}^{N_t}\gamma_{i,j,k}f_i(v_\zeta)\, g_j(v_\rho)h_k(t) \tag{24}$$

where the sets of functions $\{f_i(\,)\}$, $\{g_j(\,)\}$ are complete in $L_2(-\infty,\, \infty)$ (as in Hermite functions) and $\{h_k(\,)\}$, are complete in $L_2(0,\, \infty)$ (as in Laguerre functions). The constants $\{\gamma_{i,j,k}\}$ are fitted to the data using least squares.

(2) Equation 19 was used to obtain a smooth version of the distribution $F(v_\zeta,\, \sqrt{v_\rho^2 + v_\alpha^2},\, t)$ and Eq. 20 was used to calculate a smooth version of the function $p_{\Theta\Phi L}(\theta,\, \varphi,\, l)$.

(3) The discrete formulation of Eq. 21 was obtained in the

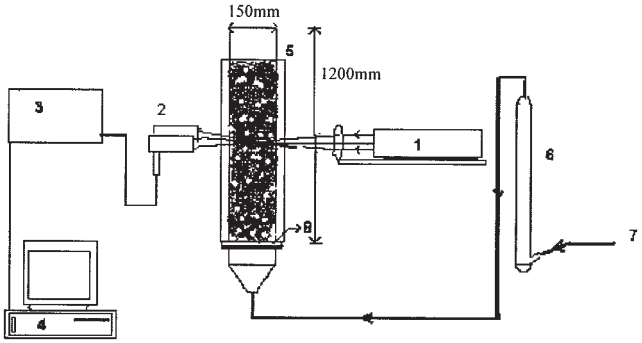

Figure 2. Experimental setup of bubble column.

1. 150 mW Ar-ion laser; 2. photomultiplier tubes; 3. LDA signal processor (BSA); 4. PC/80586; 5. bubble column; 6. soap film meter; 7. compressed air; 8. sparger.

form of discrete quantities $p_{i,k}$ and $a_{i,j,k}$ (Eq. 22), which was solved to obtain $p_{i,j}$ and obtain the size distribution through Eq. 23.

After the validation of the methodology for surrogate data, it was subjected to the actually measured experimental data to obtain the statistical distributions of the velocity values, direction θ, and the bubble passage time, which yields the chord length distribution (of projections of actual chords in axial–radial plane).

Experimental

Experiments were carried out in a cylindrical plexiglass bubble column of 150 mm internal diameter with a sieve plate (1.96 mm hole diameter) with free area of 0.25% and a single-point sparger with the hole diameter of 3.17 mm. A schematic of the experimental setup is shown in Figure 2. Simultaneous LDA measurements of axial–radial and axial–tangential velocity were made at five axial levels (H/D = 0.2, 1.4, 2.6, 3.9, and 5 away from the sparger). A 150-mW argon-ion laser was used as a source. The measurements were made after a steady flow pattern is achieved. The clear liquid height to diameter ratio was maintained at 6. At each axial level, measurements were made at several radial positions from center to wall (up to a distance of 5 mm from the wall). Close to the wall (<5 mm) the variation in beam path lengths was more and it was difficult to obtain proper intersection of all three beams at the same point. The data were collected at an average data rate of 150 Hz and 50,000 data points were collected at each position. The details about the experimental setup used and the data processing hardware are reported in Kulkarni et al. (2001a). The superficial gas velocity was maintained at 20 mm/s and the average gas hold-up was independently calculated from the difference in the clear liquid height and the dispersed height.

Although the LDA system is nonintrusive, this advantage is limited by its restrictive applicability in the multiphase systems. This is mainly because of bubble–beam interaction, which causes several problems including data corruption arising from noise and excessive scattering from bubble surface, and interruption in the intersection of all the beams at a focused measurement point. This is because bubbles may cross the laser beam and disturb the intersection of laser beams. The possible ways of bubble–beam interaction and its effect on the data rate are discussed separately in Appendix C. After data acquisition, the extent of uncorrelated features in the data (that is, noise) was reduced using a wavelet-based robust denoising algorithm discussed by Roy et al. (2000) and initially only the axial component of measured instantaneous denoised velocity data was subjected to further analysis of identification of bubble passage events using the methodology explained in Kulkarni et al. (2001a). The 2-D measurements were used to calculate the direction of bubble motion in azimuthal plane (θ). The velocity components along with the time gaps resulting from the bubble passage identified from both the time series were used as input data for the model.

Results and Discussion

We present results first for the verification of our inversion procedure with Monte Carlo simulations, followed by its use for measuring bubble size distributions in the bubble column.

Verification with Monte Carlo simulations

As pointed out earlier, the verification of our procedure for inversion of the collected data to bubble size distributions was the primary objective of the Monte Carlo simulations. Here we have tested it for (1) Dirac delta (that is, uniform bubble size), (2) Gaussian distribution, (3) exponential distribution, and (4) bimodal Gaussian distribution. For that, the surrogate data of chord length distribution obtained by following the procedure mentioned earlier, along with the corresponding velocity distributions, was used for prediction of bubble size distribution by inversion. Figures 3A–3D show the results of the above analysis. The solid line indicates the bubble size distribution used for generating chords and the resulting chord distribution is shown by the solid diamond symbol. Further, the open circles show the resulting bubble size distribution after solving the inverse problem using the chord length distribution. The results show that in all the cases of known size distribution, the inverted distribution closely agrees with the distribution used for the generation of data, where the rise angle is correlated to sizes.

Similar analysis was carried out for the data generated without any dependency of direction of motion on bubble size as for the (1) Gaussian distribution, (2) exponential distribution, and (3) bimodal Gaussian distribution. The results showed that, for this case also, the predictions (□, chord distribution; - - - predicted size distribution, in Figure 3) are in very good agreement with the assumed distribution. These results clearly reveal the robustness in the overall strategy because it is capable of inverting the two extreme cases equally well. Further, it is established here that estimation of bubble size distributions made on the basis of vertical motion alone can be seriously in error. After all, the chord-measuring device is oblivious to relative motion of bubbles and records only their absolute motion. That this is so is demonstrated below by incorporating only vertical motion, interpreting the observed chord lengths and noting the large deviation of the estimated bubble size distribution from that used to generate the data (△, predicted size distribution, in Figure 3).

Bubble size distributions in bubble column

Verification of Axisymmetry Assumptions. For our method to be applicable, it is necessary to verify the two axisymmetry

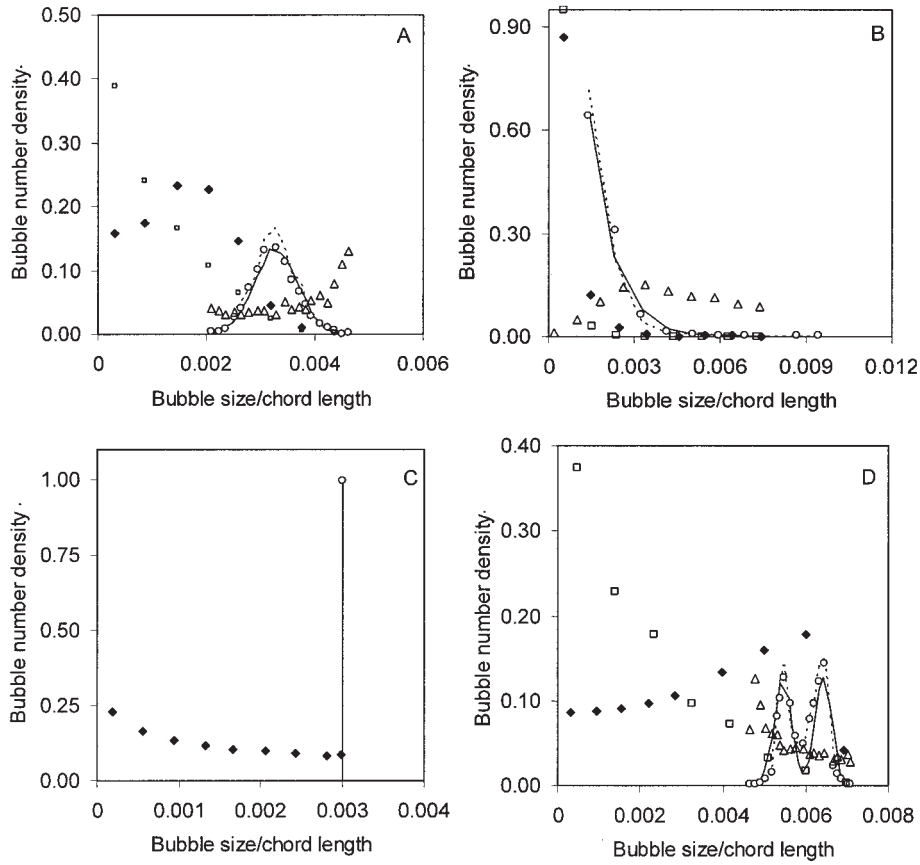

Figure 3. Resulting bubble size distribution from the surrogate data of known distributions.

(A) Gaussian distribution, (B) Dirac delta type uniform bubble sizes, (C) exponential distribution, and (D) combination of two Gaussian distributions, which is a deviation from the case of two bubble class model. (When direction of bubble motion is conditional to their sizes: ◆, chord length distribution; —, given bubble size distribution; ○, predicted bubble size distribution. Bubble motion in random directions: - - -, predicted bubble size distribution; △, predicted bubble size distribution for the case of inversion under the rectilinear motion of bubbles; and □, chord-length distribution.)

assumptions (Eqs. 5 and 14). To verify the basic axisymmetry assumption (Eq. 5) the distributions of axial and radial velocity components at several tangential positions at the same distance from the column axis were measured. Figure 4 shows (for sufficiently large data $>$ 1500 bubble events) that the time-averaged distribution of the resultant velocity vector is independent of the tangential position in the column. This observation was confirmed at several measurement levels and radial distances from the centerline. Further, it was important to check the validity of the directional distribution in real systems. In view of this, the angle made by a bubble with the column axis is calculated from the simultaneously measured two velocity components (axial–radial) at several radial positions. The results (Figure 5) showed that there exists a directional distribution of motion over the entire cross section; however, its conditionality with respect to bubble size is of prime concern for understanding the preferred directions of rising bubbles in turbulent flows. It can be seen that most of the bubbles in the central region of the column prefer to move in the range of $\pm 10°$ of vertical, that is, parallel to column axis (mainly because of the strong liquid circulation, which has upward motion in the center of column), whereas some deviations were observed at other locations. Because our model involves the directional dependency of bubble motion in the entire column, details of the same are discussed separately in Appendix B.

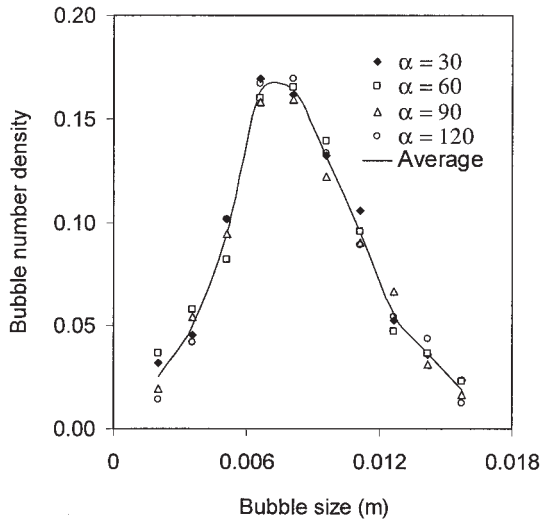

Figure 4. Experimental verification of the axisymmetry assumption.

Angles are given in degrees in the plane of column cross section perpendicular to the column axis.

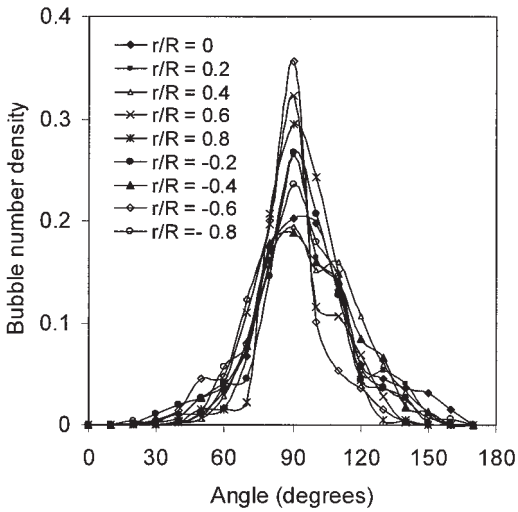

Figure 5. Experimentally observed directional distribution for bubbles rising in a bubble column.

Angles are given in degrees in the plane of column axis (90°) and with respect to the column cross section perpendicular to the column axis.

The crux of this work is based on the applicability of Abel's transform when only 2-D data are available. Although the system under consideration satisfies the condition of axisymmetry (Eq. 5), it is also necessary to check the second axisymmetry assumption (Eq. 14) or its implication appearing in Eqs. 25 and 26 below

$$p_{v_\zeta v_\rho T}(v_\zeta, v_\rho, t) = 2\int_{v_\rho}^{\infty} F(v_\zeta, u, t)\,\frac{2udu}{\sqrt{u^2 - v_\rho}} \qquad (25)$$

$$p_{v_\zeta v_\alpha T}(v_\zeta, v_\alpha, t) = 2\int_{v_\alpha}^{\infty} F(v_\zeta, u, t)\,\frac{2udu}{\sqrt{u^2 - v_\alpha}} \qquad (26)$$

Now, Eq. 16 provides for the calculation of the 3-D velocity distribution (jointly with data interruption times) from the two-dimensional velocity distribution $F(v_\zeta, u, t)$; the function $F(v_\zeta, u, t)$ is obtained by the inverse Abel's transform (Eq. 19) by using either Eq. 25 or Eq. 26. Thus it is clear that the bubble size distribution can be estimated from using either axial–radial data or the axial–tangential data. A test of the axisymmetric assumption (Eq. 14) then lies in the size distribution being the same regardless of which data set is being used. Figure 6A shows an excellent match between the results for the two sets of data. Thus the axisymmetric assumption (Eq. 14) is indeed verified in our experiments. Further confirmation of Eq. 14 can be seen from Figure 6B, which shows that the distributions of radial velocity component and the tangential components of velocity (measured independently) at a fixed location in the system are virtually the same. The validity of these observations and the suitability of the conditions for using the Abel's transform were verified at various locations in the column.

Bubble Size Distribution for Multipoint Sparger. On the validation of the main assumptions in our analysis, the experimental data for the case of multipoint sparger were subjected to the inverse methodology and bubble size distributions were obtained (Figure 7). It can be seen from the plots that, in the near-sparger region, the size distribution profiles are similar at all the radial locations of the column and the bubble size distribution was narrow compared to that at other locations. This must be mainly because of the sparger dominance in bubble formation. At higher axial levels, practically in the entire region (except one location near the wall) the distribution can be seen to have a smooth profile with a Gaussian nature. Near the wall, bimodal distribution is obtained. The latter observation is mainly an effect of the transient motion of the large-scale circulation cells that are capable of bringing a few large bubbles in the wall region along with numerous small bubbles. In fact, small bubbles could be seen in that region as they were dragged down from the disengagement zone by the liquid flowing in the downward direction along the walls. This also shows that the flow pattern in the column is not fully developed at $V_G = 20$ mm/s. The plot of average bubble size at various axial levels shows that the average size decreases from center to wall (9–6 mm) except in the near-sparger region (Figure 8). This observation can be justified by analyzing the radial profiles of the energy dissipation rates in the column. The values of energy dissipation rates were estimated from the velocity–time data using the methodology discussed by Sahu et al. (1998). The profiles at different axial positions for the case of multipoint sparger (Figure 9) showed that the energy dissipation rate increased steadily in the radially outward direction from center and showed a maximum closer to the wall. The energy dissipation rates directly reflect on the relative bubble breakup frequency and thus on the nature of bubble size profile. Thus the nature of the dissipation rate profile indicates decrease in the average bubble size from center toward the wall and it supports our predictions.

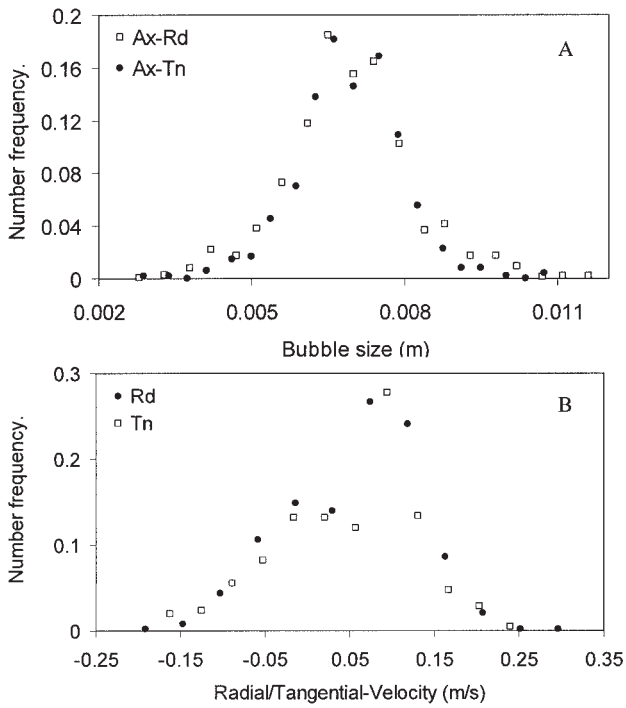

Figure 6. Experimental verification of the suitability of the data for using Abel's transform.

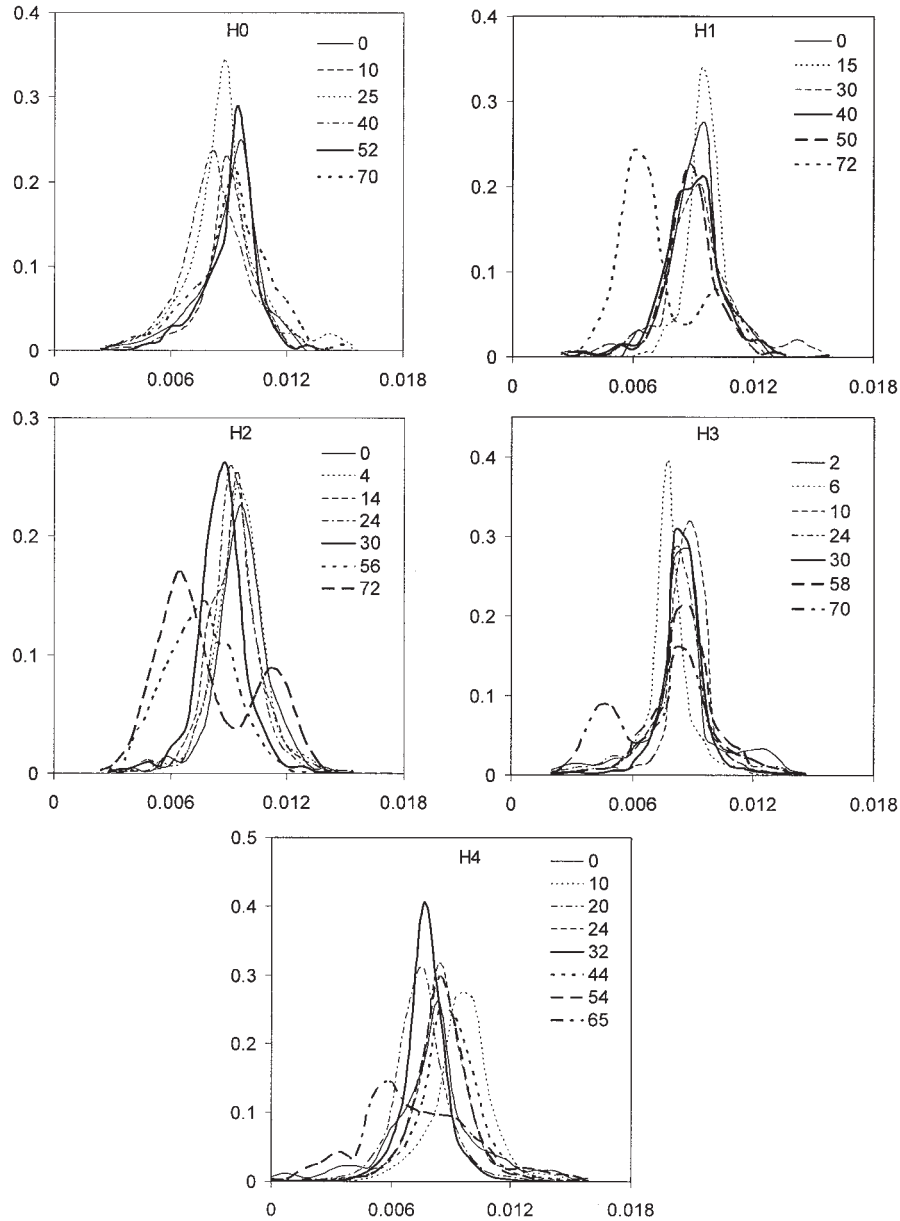

Figure 7. Predicted bubble size distribution by inversion of the experimental data of chord length distribution measured using LDA in a bubble column with multipoint sparger.

$H_0 = 40, H_1 = 210, H_2 = 480, H_3 = 590, H_4 = 750$ mm distance from sparger. Every line corresponds to a certain distance from the centerline (in mm), as indicated in the legends. Abscissa: bubble size (m); ordinate: bubble number density.

Bubble Size Distribution for Single-Point Sparger. Similar analysis was also carried out for the data from a single-point sparger at several axial and radial positions in the column. The results (Figure 10) showed that in the near-sparger region, there is a Gaussian distribution with mean close to 10.7 mm and a spread of ± 3 mm. Away from the sparger the distribution deviated from a Gaussian nature. This analysis was concordant with the visual observations where it was clearly seen that very large as well as small sized bubbles coexist in the column. However, in the bulk region of the column, the bimodal distribution is found to get smoothly transformed into the Gaussian nature as the hold-up profile in that region was fully developed. Also the average bubble size decreased to 8 mm as the larger bubbles were broken into smaller ones.

Verification of the Estimated Bubble Sizes. It is very common to formulate and use the correlations for the estimation of bubble rise/slip velocity from the available size distribution or average bubble size or from the plot of hold-up vs. gas velocity for a given system. We define the local slip velocity as the weighted average of the slip velocity distribution measured locally, whereas the average slip velocity is the area average of the local slip velocities across the cross section. In the first part, we estimated the slip velocity distribution for all the identified bubbles from the LDA data (Figure 11, for H_2, H_3, and H_4;

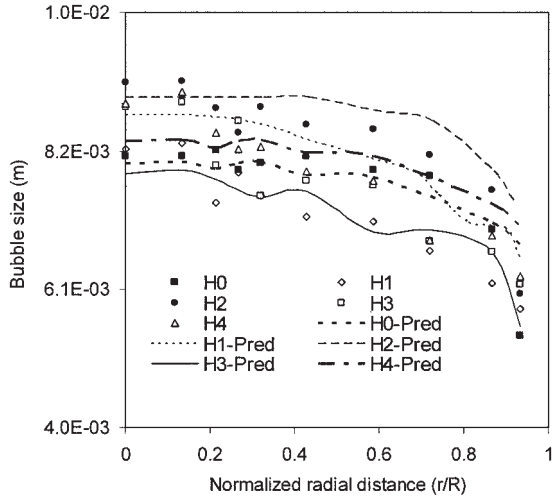

Figure 8. Radial variation of the average bubble sizes in the column.

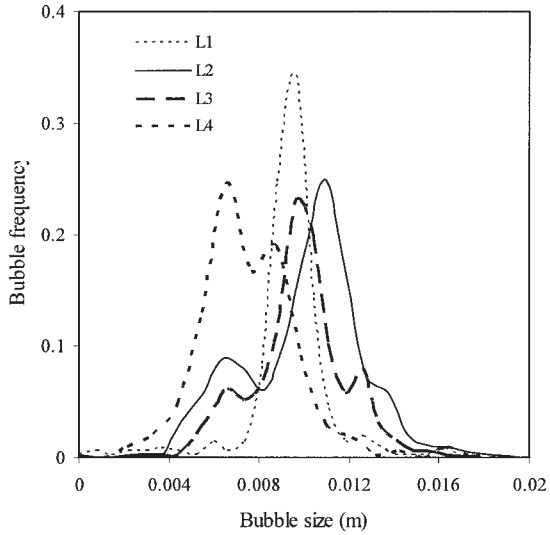

Figure 10. Predicted bubble size distribution by inversion of the experimental data of chord length distribution measured using LDA in a bubble column with single-point sparger.

$L_1 = 40$, $L_2 = 210$, $L_3 = 480$, $L_4 = 590$ mm distance from sparger. Every line corresponds to a certain distance from the centerline (in mm), as indicated in the legends.

symbols). The average measured slip velocity was found to increase with distance from the sparger (0.25–0.28 m/s).

To check the accuracy in the prediction of the bubble sizes, it was thought desirable to compare the measured axial slip velocity distribution and the slip velocity values estimated from the predicted bubble size distribution. For our case, correlation by Nguyen (1998) was used to estimate the terminal rise velocity distribution using the predicted bubble size distribution. The corresponding plots showed that the terminal rise velocities (given as a solid line in Figure 11) were noticeably smaller than the measured slip velocities (by 8–13%). This observation needs an explanation through the discussion, which follows, of the various forces acting on a bubble during its motion in stagnant liquid and in a swarm and thus on the corresponding rise velocities.

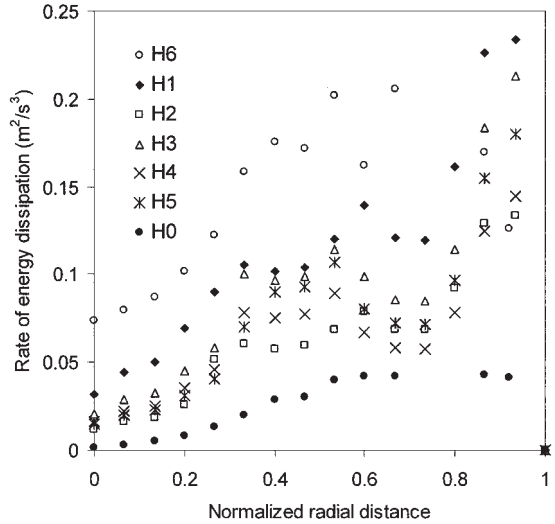

Figure 9. Profiles of energy dissipation rate in bubble column from the LDA data measured over the cross section at several axial levels given in *H/D*.

$H_0 = 0.2$, $H_1 = 1.4$, $H_2 = 2.6$, $H_3 = 3.2$, $H_4 = 3.9$, $H_5 = 5$, and $H_6 = 6.2$.

For the case of a single bubble rising in a stagnant pool of liquid, the forces acting on it are (1) buoyancy, (2) drag, and (3) gravity. The force balance (Joshi et al., 1998) shows that the drag force acting on it is proportional to the slip velocity, that is, terminal rise velocity of the bubble. In the case of a bubble column, when the bubble swarm is present the motion of a bubble again can be described using force balance. Here, the main forces, which decide the rise velocity of a bubble are (1) the buoyancy, which has an upward direction; (2) the gravity (downward direction); (3) the drag force (downward direction); (4) added mass force; (5) lift force (transverse direction); and finally (6) the form drag, which has direction toward the reduced pressure that is, along the mean flow. The contribution of the form drag and the added mass force on the bubble rise is different at different locations in the column. In the central region, with increasing distance from the sparger, the pressure acting at any point decreases and thus a reduced pressure gradient exists. This is because the bubble number density is higher in the central region, and thus the reduced pressure phenomenon is observed only in the central region of the column. The reduced pressure gradient develops pressure on the bubble surface, which is more in the direction of buoyancy and thus helps the bubble to rise faster continuously (that is, it is accelerated). Second, the added mass force acting on a bubble in the central region of the column pushes the bubble continuously in the upward direction, resulting in enhancement in its slip velocity. Thus a balance arising out of the added mass force, form drag, and the drag force on a bubble in the swarm in the central region causes it to rise faster than its terminal rise velocity. In the wall region, where the liquid has a downward flow, no such effects of reduced pressure and added mass force exist and there the bubble slip velocity is lower then its termi-

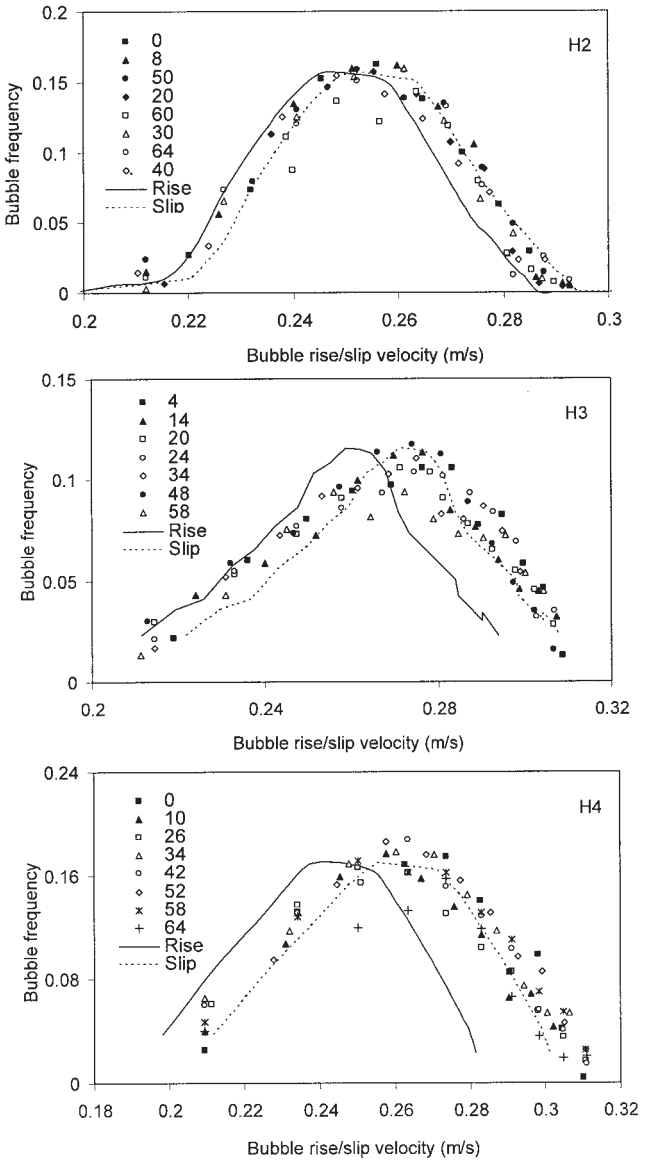

Figure 11. Estimated equivalent bubble size distribution using the axial slip velocity of bubble and the correlation by Nguyen (1998).

nal rise velocity. This discussion can be extended for estimating the slip velocity from the knowledge of the terminal rise velocity through a suitable value of the Richardson–Zaki index. Because for the nonhomogeneous systems as in the present case, the Richardson–Zaki index is less than one (which for a swarm with ellipsoidal bubbles becomes ~0.5) yields proportionality with local liquid holdup (ε_L) having a negative index. In fact, this indicates that the slip velocity of bubbles is higher than $V_{B\infty}$. Thus, the contribution of the form drag on the enhancement in the rise velocity can be taken into account by multiplying the estimated terminal rise velocity with a correction factor ($1/\sqrt{\varepsilon_L}$).

In continuation of the above discussion, we subjected the estimated rise velocity distribution for its correction using local ε_L [estimated as $(1 - \varepsilon_G)$, where local ε_G was calculated using the methodology given in Kulkarni et al. (2001a)]. The resulting average slip velocity estimated from the predicted bubble sizes is found to vary in the range of 0.265 to 0.29 m/s over different axial levels in the column. These values (given by - - - in Figure 11), compared with the experimental slip velocity distribution, showed a difference of 4–6% from the experimental values (given as symbols) at all the levels of measurement. The reason behind the difference in the values can be given in terms of the difference in the actual and the hypothesized bubble shapes we have considered in our analysis. It should be noted that in our previous analysis of the velocity–time data in a bubble column reactor it was seen that almost 90% of the bubbles are ellipsoidal in shape (Kulkarni et al., 2001c), with varying aspect ratios. However, the rise of ellipsoidal bubbles is accompanied with the oscillations and rotations, thus making both the forward and the inverse analyses intricate. The variation in the predicted average bubble size with that of the experimentally obtained size (after using Nguyen's correlation) also showed a reasonable match (Figure 8).

Further, we used the results from the analysis of drift flux model by Zuber and Findlay (1965), based on the variation in the fractional gas hold-up (ε_G) with the superficial gas velocity (V_G) for the system under consideration. The ratio V_G/ε_G was plotted against the V_G and was correlated as

$$\frac{V_G}{\varepsilon_G} = C_0 V_G + C_1 \tag{27}$$

The slope (C_0) of these plots indicates the steepness of the hold-up profile (that is, the extent of development of liquid circulation in the column), whereas the intercept (C_1) indicates the rise velocity of bubbles for average bubble size. Because the intercept is taken at $V_G = 0$, it cannot be used for the comparison with the predicted slip velocity of the bubbles at higher V_G. Thus, the slip velocity in such a case is obtained by dividing the rise velocity by the average fractional liquid holdup, which at $V_G = 0$ gives $V_S = V_G$ as $\varepsilon_L = 1$. Thus, as the V_G increases, the fractional gas hold-up increases, liquid circulation is induced in the column, and the bubbles rise at their slip velocity and not at their rise velocity. Thus, the corresponding slip velocity can be estimated as C_1/ε_L. The results (Figure 12) from our experiments showed that the average bubble slip velocity obtained from C_1/ε_L were 0.255 and 0.33 m/s for the multipoint and single-point spargers, respectively. The average slip velocities estimated from the predicted bubble sizes (after correction with local ε_L) are 0.275 and 0.342 m/s for the multipoint and single-point spargers, respectively. The predicted values are higher than the estimated values, with a difference of <12%, and the reason may be the difference in the shapes of bubbles.

These values are within an acceptable range of the values obtained from the experimental data. For the discrepancies arising in the results from our methodology (although it may not reflect noticeably on the hydrodynamics) it is required to extend the present analysis for nonspherical shapes as well for the realization of the system. This does not mean that the present analysis is misleading but, rather, needs modification in terms of geometrical realism so as to match with the actual equivalent bubble sizes of the ellipsoidal bubbles present in the system.

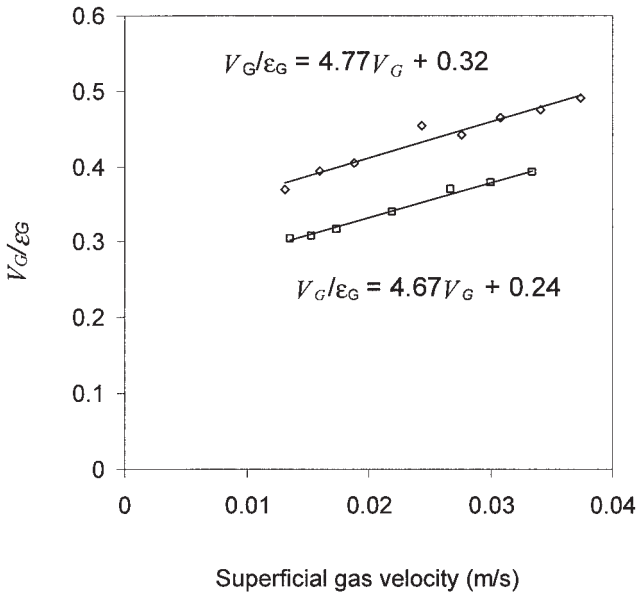

Figure 12. Plot of V_G/ε_G vs. V_G in bubble column for single-point and multipoint sparger.

Conclusions

- The axisymmetry assumptions on which the methodology presented herein rests are found to be valid, thus facilitating the transformation of chord length measurements to spherical bubble size distributions using only 2-D velocity distributions.
- The methodology is found to work well for surrogate data as well as actual experimental data from bubble columns. The validation against synthetically generated data showed that this method successfully inverts the various possible bubble size distributions and gave excellent comparison with the surrogate data for the extreme cases of dependency of direction on the bubble sizes and the random motion of bubbles, independent of their sizes.
- The resulting size distribution from the LDA data has shown that the nature of distribution is closer to Gaussian in the central region, whereas in the near-wall region it takes a bimodal shape. These results are found to match very well with the experimentally obtained size distribution estimated from the respective slip velocity distribution and this was valid even for the average bubble sizes estimated from both methods. Average slip velocity estimated for the average bubble size in the column is higher (by 11% at the most) than that from coefficients of the Zuber–Findley equation (Eq. 27). The difference could be reduced further from the knowledge of drag law for single-bubble rising in a pool of liquid and the bubble motion in a swarm. The slight difference in the estimated bubble sizes in the presence of liquid cross-flow and the predictions may be attributed to deviations in spherical shape. A better fit between the distributions obtained from inversion of chord length data and those from measurement of slip velocities would require the incorporation of corrections on both procedures. In our view, the precise transformation between chord lengths and size of nonspherical bubbles is considerably more complicated because of the possibility of rotational and oscillatory motion of bubbles; however, the estimation of bubble size through the measurement of slip velocities may be improved by including the dynamical behavior of ellipsoidal bubbles in the present model (Feng and Leal, 1997), although it is not expected to reflect substantially on the design of systems.

Acknowledgments

The authors thank the Department of Science and Technology (Govt. of India, DST/INT/US [NSF-RP061/2001]) and the National Science Foundation (INT-R0115297) for providing the financial help for this work. One of the authors (AAK) is particularly thankful to Professor M. M. Sharma Endowment for the award of Doctoral Fellowship and to the Purdue University's International Program for financial assistance during his stay at Purdue during April–June, 2002.

Notation

$C_{0,\,C1}$ = coefficients in drift flux model
D = column diameter (m)
$F(v_\zeta, u, t)$ = function used in Able inverse transform
k = turbulent kinetic energy, m^2/s^2
L, l = chord length, m
N = total number of bubbles
$p_{L(l)}$ = probability distribution for the measured chord length
$p_{L\,|\,R(l\,|\,r)}$ = probability distribution for the chord length, *conditional* on the bubble radius
$p_{R(r)}$ = distribution of bubble radii
$p_{V_\zeta V_\rho V_\alpha T}(v_\zeta, v_\rho, v_\alpha, t)$ = probability distribution function for the joint distribution of the axial, tangential, and radial bubble velocities, and the time
$p_{V\Theta\Phi L}(v, \theta, \varphi, l)$ = probability distribution function for the joint distribution of bubble velocities, direction, orientation, and the chord length
$p_{\Theta\Phi\Theta'\Phi'\,|\,R(\theta,\,\varphi;\,\theta',\,\varphi'\,|\,r)}$ = directional distribution of bubble motion conditional on its size
r = bubble radius (m), distance from the axis of the column (m)
R = bubble radius (m), column radius (m)
u_G = local axial gas velocity, m/s
u_L = local axial liquid velocity, m/s
V_G = superficial gas velocity, m/s
V_ρ = radial velocity component, m/s
V_S = axial slip velocity, m/s
V_ζ = axial velocity component, m/s
V_α = tangential/azimuthal velocity component, m/s
$\{f_{i(\,)}\}, \{gj(\,)\}, \{hk(\,)\}$ = functions defining the velocity components, and time gaps

Greek letters

α = azimuthal angle (radians)
β = angle between the bubble orientation vector and the direction vector
δ = Dirac delta function
$\varepsilon_G, \varepsilon_L$ = fractional gas hold-up and liquid hold-up, respectively
ε = energy dissipation rate, m^2/s^3
Φ, ϕ = angle made by the direction vector of bubble in the plane of column cross-section, between the line joining point P and the line of projection of vector of bubble rise
Θ, θ = rise angle of bubble in the plane of column radius and column axis
$\Theta', \theta', \Phi', \phi'$ = angles defining the bubble orientation in the column
ρ = radial distance of P from the column axis
ν_t = turbulent viscosity, m^2/s
ζ = axial position of the radial plane constituting point P

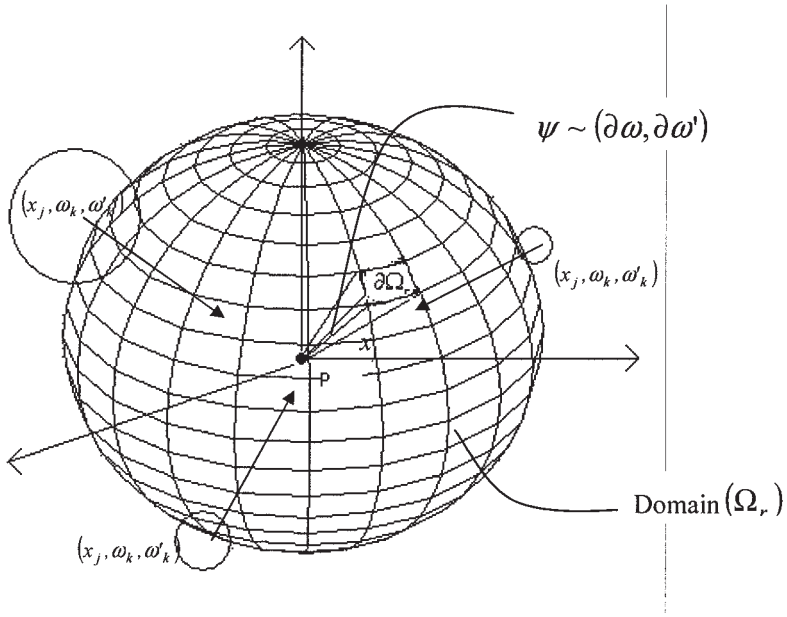

Figure A1. Schematic explaining the domain for discretization of the variables.

Literature Cited

Abel, N. H., *Oeuvres Completes*, L. Sylow, and S. Lie, eds., Johnson Reprint, New York, p. 11 (1988).

Boyer, C., A. M. Duquenne, and G. Wild, "Measuring Techniques in Gas–Liquid and Gas–Liquid–Solid Reactors," *Chem. Eng. Sci.*, **57**, 3185 (2002).

Calderblank, P. H., "Physical Rate Processes in Industrial Fermentation," *Trans. Inst. Chem. Eng.*, **36**, 443 (1958).

Cheremisinoff, N. P., "Review of Experimental Methods for Studying the Hydrodynamics of Gas–Solid Fluidized Beds," *Ind. Eng. Chem. Process Des. Dev.*, **25**, 329 (1986).

Clark, N. N., and R. Turton, "Chord Length Distributions Related to Bubble Size Distributions in Multiphase Flows," *Int. J. Multiphase Flow*, **14**, 413 (1988).

Feng, Z. C., and L. G. Leal, "Nonlinear Bubble Dynamics," *Ann. Rev. Fluid Mech.*, **29**, 201 (1997).

Ford, B., and E. Loth, "Forces on Ellipsoidal Bubbles in a Turbulent Shear Layer," *Phys. Fluids*, **10**, 178 (1998).

Joshi, J. B., "Computational Flow Modeling and Design of Bubble Column Reactors," *Chem. Eng. Sci.*, **56**(21/22), 6737 (2001).

Joshi, J. B., U. Parasu Vira, Ch. V. Prasad, D. V. Phanikumar, N. S. Deshpande, S. S. Thakre, and B. N. Thorat, "Gas Hold-up Structures in Bubble Column Reactors," *Proc. Indian Natl. Sci. Acad.* (*PINSA*), **64A**, 411 (1998).

Kiambi, S. L., A. M. Duquenne, J. B. Dupont, C. Colin, F. Risso, and H. Delmas, "Measurement of Bubble Characteristics: Comparison between Double Optical Probe and Imaging," *Can. J. Chem. Eng.*, **81**, 764 (2003).

Kulkarni, A. A., J. B. Joshi, V. Ravikumar, and B. D. Kulkarni, "Application of Multiresolution Analysis for Simultaneous Measurement of Gas and Liquid Velocities and Fractional Gas Hold-up in Bubble Column Using LDA," *Chem. Eng. Sci.*, **56**(17), 5037 (2001a).

Kulkarni, A. A., J. B. Joshi, V. Ravikumar and B. D. Kulkarni, "Identification of Principal Time Scale of a Time Series in a Bubble Column by Orthonormal Wavelet Analysis," *Chem. Eng. Sci.*, **56**(19), 5739 (2001b).

Kulkarni, A. A, J. B. Joshi, V. Ravikumar, and B. D. Kulkarni, "Simultaneous Measurement of Hold-up Profiles and Interfacial Area using LDA in Bubble Column: Predictions by Time Series Analysis and Comparison with Experiments," *Chem. Eng. Sci.*, **56**(19), 6437 (2001c).

Lim, K. S., and P. K. Agarwal, "Conversion of Pierced Lengths Measured at a Probe to Bubble Size Measures: An Assessment of the Geometrical Probability Approach and Bubble Shape Models," *Powder Technol.*, 63, 205 (1990).

Liu, W., and N. N. Clark, "Relationship between Distribution of Chord Lengths and Distributions of Bubble Sizes Including Their Statistical Parameters," *Int. J. Multiphase Flow*, **21**(6), 1073 (1995).

Liu, W., N. N. Clark, and A. I. Karamavruc, "Relationship between Bubble Size Distributions and Chord-Length Distribution in Heterogeneously Bubbling Systems," *Chem. Eng. Sci.*, **53**(6), 1276 (1998).

Magnaudet, J., and I. Eames, "The Motion of High Reynolds Number Bubbles in Inhomogeneous Flows," *Ann. Rev. Fluid Mech.*, **32**, 659 (2000).

Mclaughlin, C. M., and J. H. Rushton, "Interfacial Areas in Liquid–Liquid Dispersions from Light Transmission Measurements," *AIChE J.*, **19**, 817 (1973).

Nguyen, A. V., "Prediction of Bubble Terminal Velocities in Contaminated Water," *AIChE J.*, **44**(1), 226 (1998).

Polli, M., M. D. Stanislao, R. Bagatin, E. A. Baker, and M. Masi, "Bubble Size Distribution in the Sparger Region of Bubble Columns," *Chem. Eng. Sci.*, **57**(1), 197 (2002).

Rowe. P. N., and R. Matsuno, "Single bubbles injected into a gas-fluidized bed and observed by X-rays," *Chem. Eng. Sci.*, **26**, 923 (1971).

Roy, M., V. Ravi Kumar, B. D. Kulkarni, J. Sanderson, M. Rhodes and M. Van der Stappen, "Simple Denoising Algorithm Using Wavelet Transform," *AIChE J.*, **45**(11), 2461 (1999).

Santana, D., and A. Macias-Machin, "Local Bubble-Size Distribution in Fluidized Beds," *AIChE J.*, **46**(7), 1340 (2000).

Spelt, P. D. M., and A. Biesheuvel, "On the Motion of Gas Bubbles in Homogeneous Isotropic Turbulence," *J. Fluid Mech.*, **336**, 221 (1997).

Stravs, A., and U. V.Stockar, "Measurement of Interfacial Areas in Gas–Liquid Dispersions by Ultrasonic Pulse Transmission," *Chem. Eng. Sci.*, **40**(7), 1169 (1985).

Vicharelli, P. A., and W. P. Lapatovich, "Iterative Method for Computing the Inverse Abel Transform," *Appl. Phys. Lett.*, **50**(10), 557 (1987).

Werther, J., "Bubbles in Gas Fluidized Beds," *Trans. Inst. Chem. Eng.*, **52**, 149 (1974).

Yashikava, K., [http://www.kusastro.kyoto-u.ac.jp/~kohji/research/paper/ys1999/node2.html].

Zuber, N., and Findlay, J. A. "Average Volumetric Concentration in Two-Phase Flow System," *ASME J. Heat Transfer*, **87**, 453 (1965).

Appendix

A. Discretization of variables

As stated in the manuscript, it was assumed that bubbles are uniformly distributed in the space surrounding the measurement point P. Let us define a domain Ω_r around P and all the

bubbles that pass through P and register a chord inside Ω_r (Figure A1). Thus, a bubble situated on the *surface* $\delta\Omega_r$ of Ω_r at a distance x from point P moves toward P such that it records a chord. Thus, the initial coordinates of bubble are defined based on the distance x and the direction of the bubble's motion, that is, angles (θ, φ) and (θ', φ'), whereas the instantaneous coordinates under the condition of fixed direction of motion can be known from its velocity. In the domain Ω_r several such bubbles approach toward P and their motion can be described conveniently using the solid angles. To solve Eq. 21, because the unknowns are the discretized versions of the distributions, systematic discretization of the variables should be carried out as follows.

(1) The bubble size (R) range can be divided in M intervals (r_j, r_{j+1}) with pivots $\tilde{r}_j$, $j = 1, 2, \ldots, M$.

(2) The direction of motion, that is, the solid angle subtended by the surface $\partial\Omega_r$ about P, can be divided into K intervals. For a range of $\{0 < \theta < \pi\}$, θ has k_θ distinct elements and for a range of $\{0 < \varphi < 2\pi\}$, φ has k_φ elements, yielding total number of discretization cells $K = k_\theta k_\varphi$. Thus, the discrete solid angles must involve k_φ repetitions of each element of the θ set and k_θ repetitions of each element of the φ set. Thus for $k = (m - 1)k_\theta + l$, $l = 1, 2, \ldots, k_\theta$, $m = 1, 2, \ldots, k_\varphi$, so that the solid angle may be written as $\omega_k = \{\theta_l, \varphi_m\}$, where $\theta = [(l - 1)/(k_\theta - 1)]\pi$ and $\varphi = [(m - 1)/(k_\varphi - 1)]2\pi$.

(3) For the discretization over the solid angles $\omega_0 = \{\theta_l, \varphi_m\}$ deciding the orientation of bubble center similar strategy can be used as for the solid angles made by the direction vector.

(4) From the geometry, the position vector of bubble center with respect to P is enclosed by a solid angle $\partial\omega' = \sin\theta[\partial]\theta'[\partial]\varphi'$ and the direction vector is enclosed by solid angle $[\partial]\omega = \sin\theta[\partial]\theta[\partial]\varphi$. Further, the hemispherical solid angle pointing to point P from $\partial\Omega_r$ can have a range $\Psi \equiv \{[(\pi/2) - \theta'] < \theta < [(3\pi/2) - \theta']; 0 < \varphi < 2\pi\}$. In such a case, where $\theta > \pi$, the discrete value of θ can be assigned by replacing θ by $(2\pi - \theta)$, whereas the corresponding φ should be replaced by $\pi + \varphi$ (if $\varphi < \pi$) and by $\varphi - \pi$ (if $\varphi > \pi$).

Thus for known θ and φ, their discrete values can be determined by the corresponding indices.

B. Size dependency of bubble motion

Motion of a bubble in stagnant liquid is mainly governed by gravity, drag force, viscous force, and buoyancy. Depending on its size as well as physicochemical properties of the liquid, the direction is vertically upward in general, with a few deviations arising from oscillations or spiral movement. In a turbulent flow, the main forces that affect the bubble motion are gravity, drag, buoyancy, viscous forces, added mass force, lift force, and history or temporal memory force. Because of the turbulence in the liquid phase, the dominance of these forces varies and their effect on individual bubble changes with their sizes. For the details of individual forces acting on a bubble in a turbulent flow, the reader may refer to Spelt and Biesheuvel (1997), Ford and Loth (1998), and Magnaudet and Eames (2000). Here we address a very important phenomenon of finding the rise angle or direction of motion of bubbles in turbulent flows. The simultaneously measured axial and radial components of velocity in the bubble column enabled us to find the direction of bubble motion (θ) in the azimuthal plane. It is important to note that this angle is nothing but the projection of the actual velocity vector in the azimuthal plane constituting the column axis and radius. Because the axial component of bubble rise velocity (V_Z) is a strong function of the bubble size, the measured axial slip velocity can be correlated with the estimated rise angle (θ). Because larger bubbles will have higher buoyancy, their rise angle is close to vertical. Smaller bubbles would follow the surrounding liquid motion because their buoyancy is less compared with that of the liquid turbulence. Thus, smaller bubbles can move in any direction $\{0 < \theta < \pi\}$, whereas the larger bubbles rise in a narrow range closer to vertical. To find this exact dependency, the experimental data were correlated with the rise angle, and a third-order polynomial could be fitted to the data of 5000 bubbles from various measurement locations (Figure B1). For any value of rise velocity (that is bubble size), the value of rise angles, seen from the primary and secondary axes, gives the complete range of angles in which the bubble can rise while it is in the turbulent liquid.

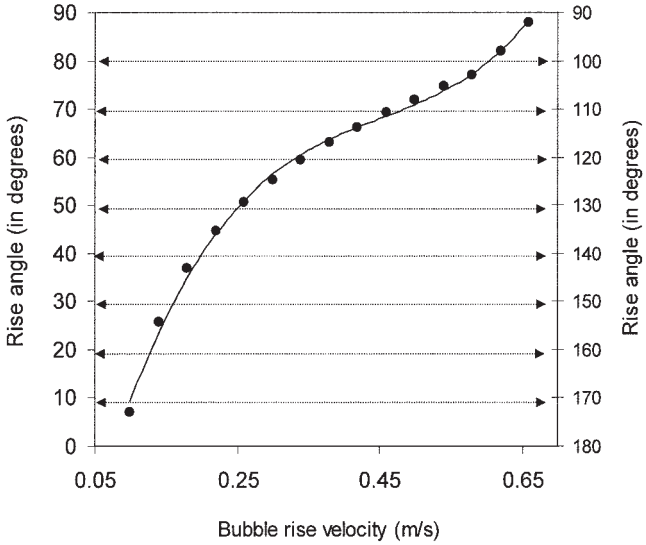

Figure B1. Dependency of rise angle on the bubble rise velocity.

The projection from the abscissa on the curve gives a point, from where the projections on ordinates on both the sides give the range of angles, in which bubble rising with a particular velocity can move.

It should be noted that at lower values of V_Z (that is, the probability of its motion in a certain direction) for smaller bubbles is always equally distributed over the whole range of rise angles, whereas it becomes narrow with increase in bubble size, making it rise rectilinearly. Thus, the liberty of bubbles to rise in any direction is constrained by its size, obviously decreasing with increasing size.

C. Modes of bubble–beam interaction during LDA measurements in a bubbly flow

As mentioned in the text, the LDA measurements in a bubbly two-phase flow are relatively difficult when compared with those in the single-phase systems. The data are obtained only when the beams intersect in the liquid phase at a fixed location and, unlike in single phase, it creates complexities in

the data processing and interpretation. One of the main reasons behind the intricacy in data analysis is the interaction of gas bubbles with the beams, which results in time gaps in the data (that is, no data are obtained). Apart from these gaps in the data, another unwanted feature is the corruption of the data resulting from the secondary scattering from the surface of bubbles, thus generating noise. The noise in the signal can be discarded using excellent denoising techniques, thereby producing a noise-free signal with time gaps arising from bubble–beam interaction.

Because of the presence of gas bubbles, two types of bubble–beam interactions are possible:

(1) Crossing of one or both the beams by a gas bubble in the beam path before and after the point of intersection. There is a possibility of multiple bubbles crossing in both beams.

(2) Blocking of the measurement volume itself by the bubble.

In our method, the criterion that gives an idea about the passage of a bubble through the measurement volume is based on either the value of cross-correlation (from the cross-correlation method, which uses two simultaneously measured velocity components) or the energy burst identified using multiresolution analysis (of axial velocity component) along with the value of slip velocity measured in the immediate vicinity of the bubble. The, the slip velocity value directly gives an indication about the passage of a bubble through the measurement point. It may again be emphasized that when the bubble passes through the beam intersection, all the criteria—that is, cross-correlation, energy burst, and slip velocity—are satisfied. In contrast, if there is a time gap because of bubbles crossing the beams anywhere else then the above criteria are not satisfied. Thus the entire measurement time was clearly divided into (1) time when gas phase was present at the measurement point and (2) time for which gas phase was not present at the measurement point and therefore this time was assigned to the liquid phase. The detailed procedure of the same is discussed in Kulkarni et al. (2001a). Because the clear identification of the time segments are possible for the presence of gas and liquid phases, the time that indicates passage of bubble through the measurement point was used for the estimation of chord length distribution in our analysis.

Manuscript received Sep. 11, 2003, and revision received Mar. 24, 2004.